Advances and Challenges in Understanding the Microscopic Structure-Property-Performance Relationship in Perovskite Solar Cells

Yuanyuan Zhou[1,2,*], Laura M. Herz,[3,4] Alex K-Y. Jen[5,6], Michael Saliba[7,8]

[1] Department of Physics, Hong Kong Baptist University, Kowloon, Hong Kong SAR, China; https://orcid.org/0000-0002-8364-4295

[2] Smart Society Lab, Hong Kong Baptist University, Kowloon, Hong Kong SAR, China;

[3] Department of Physics, University of Oxford, Clarendon Laboratory, Oxford OX1 3PU United Kingdom; https://orcid.org/0000-0001-9621-334X

[4] TUM Institute for Advanced Study, TU Munich, 85748 Garching bei München, Germany

[5] Department of Chemistry, City University of Hong Kong, Kowloon, Hong Kong SAR, China; https://orcid.org/0000-0002-9219-7749

[6] Hong Kong Institute for Clean Energy, City University of Hong Kong, Kowloon, Hong Kong SAR, China

[7] Institute for Photovoltaics, University of Stuttgart, Stuttgart, Germany; https://orcid.org/0000-0002-6818-9781

[8] Helmholtz Young Investigator Group FRONTRUNNER, IEK5-Photovoltaik, Forschungszentrum Jülich, 52425 Jülich, Germany

Correspondence should be addressed to: yyzhou@hkbu.edu.hk

Abstract

The emergence of perovskite photovoltaic technology is transforming the landscape of solar energy. Its rapid development has been driven by the advances in understanding of thin-film microstructures of metal halide perovskites and their intriguing correlations with optoelectronic properties, device efficiency, and long-term stability. Herein we discuss the morphological characteristics of three key microstructure types encountered in perovskites that include grain boundaries, intragrain defects, and surfaces. Revealing detailed structural information of these

microstructure types via tailored characterizations is crucial for probing their detrimental, neutral, or beneficial effects on optoelectronic properties. We further elaborate the impacts of these microstructures on degradation of perovskites. Representative examples are also presented, which have translated fundamental understandings to achieve state-of-the-art perovskite solar cells. Finally, we call for attention on probing hidden microstructures, high-spatiotemporal-resolution characterizations, and harnessing the potential merits of microstructural imperfections towards an elevated understanding of microstructure-property-performance relationship for the next solar cells advance.

1. Introduction

The need for decarbonizing our current energy generation has driven an intense search for novel photovoltaic (PV) technologies that can deliver high power conversion efficiencies (PCEs) at low manufacturing cost. In 2009, Miyasaka and coworkers[1] reported for the first time a type of PVs using metal halide perovskites (MHPs). The subsequent use of MHPs in engineered thin-film device structures has triggered excitement, leading to the advances in perovskite solar cells (PSCs) with PCEs now reaching certified 25.7% and excellent stability parameters approaching industrial standards.[2-13] A typical PSC consists of a centre layer of MHP sandwiched by an electron-transport layer (ETL) and hole-transport layer (HTL) (**Figure 1a**).[14] MHPs generally adopt the ABX_3 structure (**Figure 1b**), where A is an organic cation such as methylammonium (MA^+), formamidinium (FA^+), or Cs^+; B is Pb^{2+} or Sn^{2+}; and X is I^-, Br^-, or Cl^-. The family of MHPs are now extended to embrace lower-dimensional members with tailored crystallographic structures,[15] offering intriguing optoelectronic properties and stabilities. This unlocks a wide material range for optimizing both single- and multi-junction PSCs in addition to opening novel fundamental questions.

For any given MHP, microstructure is the most critical factor determining properties and thus device performance.[16] For PSCs, the most straightforward performance parameters are PCE and stability. PCE is a product of open-circuit voltage (V_{OC}), short-circuit current density (J_{SC}), and fill factor (FF) measured under one-sun illumination. All three parameters are affected by photocarrier transport and recombination processes in MHPs, and they are intimately related to the microstructure.[17] Regarding the PSC stability, the key challenge is the relatively low materials stability of MHPs under external stimuli such as heat, moisture, oxygen, and electric fields,[17] which is related to the microscopic transport of intrinsic and extrinsic ionic/molecular species in MHP films. In addition, the (opto)mechanical reliability of perovskite which is microstructure-dependent can influence PSC stability.[18] Therefore, it is unsurprising that the technological advances in PSCs have been largely driven by improved understanding and rational engineering of the MHP microstructure and associated morphological defects, as illustrated in **Figure 1c** (see **Box 1** for a discussion on the figure details).[16,17,19] In fact, MHPs exhibit an unconventionally variable microstructure, regarded as both a blessing and a curse: while the extremely facile processability of MHPs opens the door to wide yet precise control

over microstructure features, the soft nature of MHPs renders their deterministic characterizations challenging.[15,16] The coexistence of opportunities and challenges has stimulated intense research aiming to unravel the intriguing structure-property correlation for revealing mechanistic origins of PSC efficiency and stability losses.[15,20,21]

This review groups performance-limiting microstructural features into three types on the basis of where morphological defects extend in MHP thin films: grain boundaries (GBs),[17,22-26] intragrain defects (IGDs),[19,27,28] and surfaces [11,29-33]. By examining updated findings from recent representative studies related to these three microstructure types, we herein create a unique knowledge hub that connects four key aspects of previous perovskite research works: characterization techniques, structural variations, properties, and device performance. Meanwhile, we provide insights into these findings that not only evoke classical materials theories but also expand the territories of materials and energy sciences. Specifically, first, we review recent advances in morphological characterizations of the three MHP microstructure types. The unique capabilities of various powerful microscopic characterization tools are leveraged to yield reliable, complete imaging of these microstructures. Then, we discuss the effects of these microstructure types on photophysical properties of MHPs, followed by an elaboration on their impacts on degradation modes of MHPs with examples on state-of-the-art PSCs achieved via translating such fundamental understandings. Finally, we present perspectives on emerging directions for addressing the missing yet critical information on the microscopic structure-property-performance relationship of MHPs for further technological advances of PSCs.

2. Morphological Characteristics of MHP Microstructures

Microstructure is defined as structural or chemical inhomogeneities that are formed by spatially distributed components that differ from the perfect crystal lattice.[34] In modern materials science, microstructure has encompassed the length scales of micrometres down to (sub-)nanometre with the advance in microscopy. Numerous characterization effort has been invested to unravel the microstructural details of MHPs, featuring a range of unique characteristics distinguish MHPs from conventional semiconductors.[16,17,19,35]

2.1. Grain boundaries

The MHPs in state-of-the-art PSCs possess a polycrystalline microstructure with crystal grains of microscale sizes. GBs are the most studied microstructural feature so far, not only because of their prominent existence and confirmed effects on properties but also owing to the relative ease in identification and characterization as compared to IGDs and surfaces.[16,36] Usually MHP GBs are identified based on their grooving morphologies developed during solution processing.[37] The GB characteristics proven to influence the PSC behaviour are density and groove angle on the film surface. GB density corresponds to the average grain size, which can be qualitatively examined using scanning electron microscopy (SEM; **Figure 2a-c**). It statistically reflects to which extent light and charge carriers may be scattered in an MHP film. It is generally revealed that a reduction in GB density, concluded from the SEM observation,

can generate an overall positive effect on PSC performance. Regarding GB groove angle, it is measurable based on the surface topography profile acquired using atomic force microscopy (AFM; **Figure 2d-f**). GB grooves can not only potentially lead to imperfect contacts between MHP and other layers but also trap solvent and moisture, impacting physical and chemical properties at the film surface/interface. Nevertheless, SEM and AFM only provide basic morphological characteristics of GB while more qualifiable characteristics, including degree of disorder, number of coincidence site lattice (sigma values), crystallographic directions for GB tilt/twist classification, specification of grain boundary planes, and exact chemical compositions, have to be resolved by knowing relevant atomic information. Transmission electron microscopy (TEM) of MHPs is therefore explored with mixed success.[38] This is primarily due to the relatively high beam sensitivity of MHPs that not only prevents TEM observations with normal electron dose but also challenges the acquisition of focused-ion-beam (FIB) based sample specimens. While the field is still in the process of exploring optimal specimen-preparation and imaging methods, by leveraging low-dose scanning TEM (STEM), atomic-scale structural information of perovskite microstructures has been imaged in directly-deposited and FIB-ed MHP film sample specimens (**Figure 2g-i**), offering plan- and cross-section views, respectively.[19,39] In particular, Rothmann *et al.*[19] show that in an evaporated $FAPbI_3$ MHP thin film, while many GBs are highly crystalline with a low degree of disorder, there are other GBs that are highly disordered. Such atomic-scale structural variations between different GBs suggest one possible origin of the discrepancy on the GB effects on MHP properties.[19] In fact, the variation of the local (dis)order of GBs has been widely studied in other materials systems, but the inclusion of organic cations differs MHPs, and how the organic-inorganic complexation affects the local (dis)order of GBs remains unknown, pointing to a fascinating area in fundamental materials research.

While tailored TEM characterization provides both plan and cross-sectional views of GB structures in MHP films, GB network in practical PSCs can be even more complex to assess. The MHP layers in state-of-the-art PSCs are as thick as about 1 μm, as compared to the 10 nm thick thin films studied by Rothmann *et al.*[19] In such films, GBs can be frequently buried (**Figure 2j**), preventing regular surface-based observations and calling for tomographic techniques. In this context, a new tomographic AFM method is developed, entailing a high load applied to the conductive AFM tip to probe and to instantaneously polish the film surface for exposing the buried bulk features.[40] By acquiring numerous 2D maps at increasing film depths, 3D film tomography is then constructed to present a view of 3D GB network as reflected by the photoconductivity contrast. As seen in **Figure 2k**, buried GBs can present a different distribution from that from top-view and usually the GB density in the near-bottom region is higher. This is a critical finding, as the bottom side is where the light illuminates during PSC operation and these buried GBs may exhibit more influence than bare GBs on the optical, electronic, and chemical properties of MHPs. This concept of tomographic imaging may be extended to TEM,[41] which can potentially yield 3D images with atomic details.

Another important geometric parameter of GBs is misorientation angle, which describes the relative orientation of two crystal grains with respect to each other by either tilting or twisting (**Figure 2l**). The misorientation can reflect the structural coherence of two crystalline planes, and therefore, it will affect the atomic-scale interaction of GBs with electronic carriers, ions, and molecules in MHPs. While Kelvin-probe force microscopy (KPFM) [42] is a feasible method for qualitatively differentiating low-angle and high-angle GBs based on the surface potential contrast, electron back-scattering diffraction (EBSD) is the workhorse for accurate quantification of GB misorientations over thin films. In fact, the EBSD characterization of perovskites was not considered successfully until the recent use of low-dose, high-sensitivity detector.[43] **Figure 2m** shows a typical inverse pole-figure map of a $MAPbI_3$ MHP film acquired using EBSD. Jariwala *et al*. [43]showed that a higher spread in misorientation within MHP films leads to more severe non-radiative carrier recombination, mostly related to the increase in local strain heterogeneity.

2.2. Intragrain Defects

IGDs have started to draw attention in the field, as it is frequently observed that reducing GBs does not necessarily result in PSC performance enhancement.[39] The relatively frequent existence of IGDs in MHPs is attributed to the softness of crystal lattice that allows high tolerance to local disorder within crystalline grains. While considered electrically active, IGDs are rarely visible under regular SEM or AFM, for which their effects have been omitted. Nevertheless, the advance in TEM of MHPs have facilitated the confirmation of a range of IGDs types,[19,44,45] including coherent twinning boundaries (CTBs), stacking faults (SFs), dislocations, and point defects (**Figure 3a-e)**.[19]

CTBs refer to the special boundary formed between highly symmetry lattices (**Figure 3f**). one possible formation mechanism of CTBs in MHPs is based on the facile polymorphic transformation occurring in the grain interior during film processing or upon device operation. For instance, $MAPbI_3$ perovskite can exhibit a cubic-to-tetragonal phase transition near 50 °C when cooled from a typical processing temperature over 100 °C. The twin domains formed as such can extend across the whole crystal grain with a few hundred nanometres wide. It is revealed that they reversibly (dis)appear across the tetragonal-to-cubic phase transition temperature, attesting the proposed formation mechanism.[44] In addition, the crystallographic structure of these twins is usually found consistent with the classic 90° *a-a* domains that are formed in barium titanate perovskite via similar phase-transition processes.[44,46]

SFs refer to those planar defects in which the proper order of stacking planes is interrupted, whereas two unconventional types of SFs have been identified in MHPs. The first is Ruddlesden-Popper (RP) fault, which is chemically expressed as $(AX)(ABX_3)_n$ ($n = \infty$) and usually observed in inorganic MHP nanocrystal-assembled films.[45] One intriguing structural feature of RP faults is that they can extensively propagate within MHP grains and frequently form right-angle steps. This creates unusual intragrain interfaces with added structural dimensionality. The tolerance to such kinked stacking faults may be attributed to high internal

strain in nanoscale MHP domains. The other type of MHP SFs are structurally formed by a partial shift of adjacent crystal planes, exhibiting a limited dimension of a few tens of nanometres and cannot form kinks (**Figure 3g)**.[19,39] Their formation of these SFs is mostly related to MHP synthetic conditions, as there is evidence showing their density is tailorable via post-treatment.[47] The morphological difference between the two SF types could lead to different effects on photocarrier transport and stability.

Dislocations (1D) and point defects (0D) are lower-dimensional defects that can be intrinsically formed in MHPs or easily created during device operation. Compared with GBs, CTBs, and SFs, the lower dimensionality of these defects may cause relatively localised effects on properties. In particular, dislocations may form channels of higher conductance in MHP films, which can be harnessed for tailoring film carrier mobilities.[48] Also, dislocations and point defects are relatively mobile. Upon external stimuli such as electrical field, light, strain, and thermal conditions, they can interact with 2D crystallographic defects including GBs, CTBs, and SFs, forming charge-carrier traps and adding to the complexity in degradation modes.[39] In general, characterizations of dislocations and point defects in MHPs are even more challenging due to the structural dimension encountered and strict sample geometry required.[19,38] While the atomic morphologies of edge dislocations (**Figure 3h)** and vacancies (**Figure 3i)** of certain types have already been experimentally confirmed in the MHP films ($FAPbI_3$),[19] screw dislocations and interstitial ions haven't been imaged yet, leaving vast space for future discoveries.

Unlike the case of GBs, reports on MHP IGDs tailoring are rare, whereas a recent study by Li *et al.* has proven its feasibility via both composition and processing engineering. **Figure 3j** show TEM images of $MA_{1-x}FA_xPbI_3$ MHPs with x varying from 0 to 1.[47] In $MAPbI_3$, $\{112\}_t$ CTBs (determined based on electron diffraction pattern) are observed in almost all grains, which are reduced to only half when 10 mol% FA is incorporated. When x is further increased, all $\{112\}_t$CTBs will basically disappear whereas a different type of CTBs or SFs start to emerge with $\{111\}_c$ boundaries. Furthermore, Li *et al.*[47] showed the preparation methods influence the formation of IGDs. Solution-processed $MA_{1-x}FA_xPbI_3$ ($x \geq 0.5$) MHPs can show much higher density of $\{111\}_c$ IGDs than that of a thermally evaporated $FAPbI_3$ MHP film. Post-treatment of MHPs using methylammonium-thiocyanate vapour annealing can also change the $\{111\}_c$ IGDs density. By combining continuous tailoring, density qualification, and type determination of various IGDs, systematic investigation on intriguing IGDs effects on various MHP properties and PSC device parameters is demonstrated, featuring an overall negative role for as-mentioned IGD types in this study (**Figures 3k-l**).

2.3. Surfaces

The top and bottom surfaces of MHP films (**Figure 4a**) interact directly with other device layers and the environment. Thus, they exhibit a strikingly enhanced role on properties due to the nanoscale film dimension as compared to those in bulk materials where GBs and IGDs microstructures dominate. Therefore, surfaces are discussed as another prominent MHP

microstructure type in PSCs.[49,50] In particular, MHP surfaces accommodate intriguing microstructural dynamics that involves the interplay between photo-physics and chemistry, as they are formed upon continuous interactions of MHPs with the external environment during processing and later determine the interactions between the MHP layer and ETL/HTL. In this context, the structural characteristics of MHP surfaces with be determined by two aspects, one concerning intrinsic characteristics while the other concerning interface structures when they form junctions with other device layers. Both will potentially influence the transfer of photocarriers with critical impacts on device currents and voltages.[33] MHP surfaces are also a stability-limiting factor as they favours ionic interactions and movement.[51,52]

The intrinsic characteristics of MHP surfaces feature crystallographic facet, chemical termination, and surface point-defects. Determining the crystallographic facet of MHP grain surface is necessary because the properties and structure within any given grain are not fully isotropic. It is unambiguous that statistical manipulation of orientations of MHP grains can yield improved properties, microscopic studies elucidating the role of local surface facets await further advances in EBSD qualification of MHP films. For chemical termination (**Figure 4b**), it has been extensively studied theoretically, but the experimental determination on chemical termination in MHPs has not been established until the appearance of solid-state nuclear magnetic resonance (ssNMR) characterization of MHPs.[53,54] Using ssNMR, the binding sites and modes of ligands at the surface are probable. Surface termination in MHPs is known sensitive to synthetic conditions.[55] Yuan *et al*.[56] showed that the use of N,N-dimethylformamide and dimethyl-sulfoxide solvent atmosphere can convert PbI_2 termination to AX termination in MHPs *via* Lewis-base interaction, thereby transforming the surface electronic landscape (**Figure 4e**). With regard to surface point-defects (**Figure 4c**), they are visible under scanning tunnelling microscopy,[57] and they exist prominently in MHPs mostly for two reasons: (i) the relatively soft ionic bonds in MHPs can easily create incompletely coordinated sites; (ii) surface structures are quantum-confined, allowing higher tolerance of morphological defects. These surface point-defect types can include iodide vacancies, lead antisites, and organic-cation vacancies, creating in-gap states and thereby reducing device voltage. One generic method to engineer the surface point-defects is to incorporate a molecular-functionalization layer via solution processing, which actively interact with defects and make them benign (**Figure 4d**). Successful passivators reported so far include organic-molecules, inorganic salts, and organic-inorganic hybrids. **Figure 4f** is an example for such showing phenethylammonium-passivated $FAPbI_3$ that can enable state-of-the-art PSCs.[10] Furthermore, chemical termination of MHP surfaces can be actually closely associated with the density of surface defects,[24] and thus engineering strategies of chemical termination and surface point-defects, as well as crystallographic facets, may be coupled towards the best-performing PSCs.

Heterointerfaces of two types have been recently created as novel MHP surface structures to achieve state-of-the-art PSCs, as they can potentially mitigate the issue associated with regular surface treatments which inevitably introduces a high degree of structural disorder. For type-I heterointerfaces, we specifically point to those coherent interfaces formed between MHPs with

different dimensionalities (**Figure 4g**). Such surface structures can be controllably formed via treatment of surfaces with solutions containing bulky or lengthy organic cations, followed by a post-treatment **(Figure 4i**), which induces the formation of 2D Ruddlesden-Popper or Dion-Jacobson MHP layers. The dimensionality of 2D MHP fragments is found essential to optimizing the passivation effects on both electron- and hole selective interfaces, which can be controlled either via post-treatment conditions or incorporated organic cations. Zami *et al.*[58] showed that all 2D perovskite passivation layers prepared through thermal annealing creates mostly n=1 phase while the formation of $n \geq 2$ phases became more pronounced when the room-temperature post-treatment was performed (**Figure 4j**). Chen *et al.* [59] showed that bulkier organic cations lead to high-*n* 2D MHP surfaces. These studies by Zami *et al.* and Chen *et al.* enable highly efficient and stable PSCs in normal and inverted architectures, respectively. For type-II heterointerfaces, they are fabricated via an epitaxy growth of a coherently heterolayer on top of MHPs (**Figure 4h**), which significantly enhance interface integrity and stability. This can be attributed to the introduction of interfacial strain that suppresses defect migration, thus beneficial to device performance. Such heterointerfaces can be achieved by the reaction between MHP precursor and pre-buried additives in as-deposited charge-transport layer (**Figure 4i**). Min *et al.*[13] showed a coherent interlayer of $FASnCl_x$ via chemical reaction between a Cl-containing $FAPbI_3$ MHP film and a Cl-bonded SnO_2 ETL (**Figure 4k**), which is found to substantially reduce the photocarrier recombination near the interfacial region while minimally affecting the conduction of extracted electrons. Correspondingly, a certified PCE as high as 25.5 % is reported based on this heterointerface.

3. Local photophysical properties of MHP microstructures

Having developed the capability for revealing morphological characteristics of MHP GBs, IGDs, and surfaces, the field becomes interested in unravelling their impact on photocarrier transport at the microscopic scale based on the local profiles of electronic structures at these microstructural features in the general context.

At GBs, various point defects aggregate and induce self-doping, causing simultaneous shifts of the conduction band minimum (CBM) and valence band maximum (VBM), *i.e.* energetic band bending. Self-doping to positively or negatively charged GB states will induce downward or upward band bending of both CBM and VBM, respectively. Such band bending creates beneficial effects by facilitating the collection of one type of photocarriers whereas the other repelled. In **Figure 5a**, the scenario of downward band-bending is illustrated, which appears to be the case frequently encountered in MHPs. Nevertheless, CBM lowing can also cause the V_{OC} drop as the fermi level tends to shift towards in-gap states. Furthermore, GBs can introduce abundant in-gap trap states, further accelerating non-radiative recombination. deQuilettes *et al.*[60] performed correlated PL-SEM characterizations to spatially resolve the PL decay dynamics in $MAPbI_3$ films, which reveal lower-intensity PL and shorter PL lifetime at GBs compared with grain interiors. To further in-situ visualize the photocarrier diffusion across GBs, Li *et al.*[61] developed a wide-field PL distribution method (**Figure 5b**) to directly observe carrier diffusion. The results indicate GBs efficiently block the photocarrier transport (**Figure 5c**),

affirming the overall negative role. Nevertheless, the role of GBs in MHPs is still being debated, with some reports conversely showing that GBs could be neutral or even beneficial.[40,62,63] Such discrepancies in the properties of MHP GBs may be related to a real spread in their detailed characteristics and electronic properties, as well as uncontrolled variations in IGDs and surfaces.

In contrast to GBs, IGDs lead to obviously different influences on energetics of MHPs. For CTBs, due to its high symmetric structure, they induce minimal self-doping under static conditions, imparting negligible effects on band alignment and photocarrier transport (**Figure 5d)**. Xiao *et al.*[28] assembled a setup of scanning photocurrent microscopy that records a lateral linear profile of local laser-excited photocurrents across a CTB-containing crystal sample (**Figure 5e)**. The results show linear photocurrent profiles across the two electrodes at all bias voltages (**Figure 5f)**, reflecting the neutral role of CTBs on photocarriers. Nevertheless, the atomic structures of CTBs are not fully confirmed using STEM in this study, and thus, we should revisit such experimentally observed CTB effects. Furthermore, in the case of mixed-halide MHPs, CTBs can become nucleation centres for phase segregation, forming I-rich clusters to serve as a potential well or barrier for the carrier transport depending on the bulk bandgap.[64] For SFs, the missing of crystal planes or the shift of plane can enlarge the atomic distance, creating larger bandgap locally, *i.e.* CBM upward shift and VBM downward shift (**Figure 5g**). As a result, a semiconductor-insulator-semiconductor junction will form and repel photocarriers. Thind *et al.*[45] theoretically studied a RP fault in $CsPbBr_3$ based on a model equivalent **(Figure 5h)** to the STEM-revealed atomic structure, which induces no deep defects due to the absence of Pb dangling bonds or Pb-Pb bonds. **Figure 5i** shows the band diagrams obtained through a layer-by-layer projection of the density of states, showing band offsets consistent with the CBM/VBM charge density. We hypothesize that the role of RP faults on charge-carrier transport in PSCs may be dependent on their geometrical distribution and its effects on charge percolation pathways to extraction layers. In contrast to the RP fault, other types of stacking faults are experimentally found to negatively impact the photocarrier lifetime and device parameters, which is mostly related to the different atomic and bonding arrangement between different types of SFs.[47] Nevertheless, one urgent need is to enable experimentally microscopic observation on individual SFs of each types and their local correlation with (opto)electronic properties. This is challenging since these SFs are completely invisible to other characterizations. We are therefore devoting effort to developing *operando* TEM characterization with the integration of an optoelectronic microelectromechanical system (MEMS) chip to visualize the device operation in the presence of IGDs under TEM.

For surfaces, both lateral and vertical energetic profiles are critical to PSCs. Laterally, any heterogeneity in crystallographic facets, chemical termination, and point-defect accumulation will lead to heterogeneity in electrical activities, which can occur at the grain or subgrain scale. In this regard, VBM and CBM profiles on pristine MHP surfaces grown from solution are supposed to form irregular steps with relative local energy levels influenced by corresponding structural characteristics (**Figure 5j)**. Leblebici *et al*.[33] used a conductive AFM setup (**Figure 5k**) to map the photoelectrical response of grain surfaces, finding spatially correlated

heterogeneity in J_{SC} and V_{OC} within individual grains (**Figure 5l).** These variations have also been linked to crystallographic facets at the nanoscale. While there is still no systematic investigation to correlate surface termination and point-defect accumulation with properties, theory-guided experimental efforts have demonstrated uniform tailoring of surface characteristics can lead to absolute device improvement, attesting their important role. Then, assuming that we have achieved a lateral homogeneity in energy level on an MHP surface via passivation, the vertical energy level alignment across the MHP bulk, surface, and ETL/HTL (**Figure 5m**) becomes another limiting factor, as some passivation could cause a negative work function change which drives the formation of a potential well and the accumulation of charges, This drives the halide migration and affect carrier dynamics as well as device stability. Tan *et al.*[65] showed a modification in the surface treatment method by using OATsO instead of commonly used OAI can upshift the vacuum level and minimize the potential well to mitigate the charge accumulation issue, which is confirmed by KPFM surface potential measurement. (**Figure 5n-o**).

4. Degradation modes of MHP microstructures and their device impacts

The most general degradation mode in MHPs is related to the highly volatile nature of organic cations and halide anions, which converts perovskites into PbI_2 or metallic Pb.[66] This is regardless of compositions. Since the movement and removal of these intrinsic ions have to involve breaking of their bonds with the MHP matrix, it is hypothesized that such degradation will be initialized in those microstructural regions in which more dangling or wrong bonds are accommodated.[67] This can be supported by systematic X-ray and optical characterization studies showing MHPs with increased population of GBs, IGDs, and surfaces.[17] While the nucleation of degradation in these three types of microstructures can be similar, specific degradation modes are varied according to their inherent structural dimensionalities (**Figure 6a**).

GBs are interconnected through bulk films, forming 3D complex network. Thus, the decomposition can propagate in relatively facile paths, leading to rapid degradation throughout film bulk. However, IGDs are usually separated from each other in the MHP film. Once degradation occurs, its propagation is expected to be localized. For the surface case, the degradation can occur in the 2D manner, and it can be less constrained compared to that via GBs and IGDs. This implies that different perspectives are needed for engineering GBs, IGDs, and surfaces to improve the MHP stability. *In-situ* TEM imaging is desired for experimental exploration of degradation mechanisms, which have been used tentatively. Alberti *et al.*[68] acquired a sequence of TEM images of an $MAPbI_3$ film sample in real time, finding metallic Pb clusters initially formed at GBs trigger the perovskite degradation and then migrate preferably along GB network. It is of intrigue that these Pb clusters frequently aggregates at the centres of triple-junction GBs, possibly related to the low energy states offered by that triple-junction geometry. This features the role of detailed GB characteristics on MHP degradation mechanism. Alberti *et al.* also found, in some cases, the Pb also apparently migrates inside the grains, which could be attributed to the presence of unrevealed IGDs. While it is also possible

metallic Pb clusters can be formed under e-beam and vacuum, Alberti *et al.* have carefully excluded these effects by performing control experiments, which is important for *in-situ* TEM studies of MHPs due to their beam sensitivities.

Beyond phase decomposition, a multitude of other composition-dependent mechanisms can affect the MHP stability.[69] We will then discuss the role of microstructure on the stability of state-of-the-art MHPs of different types separately: median-bandgap $FAPbI_3$,[70] wide-bandgap mixed-halide MHPs,[71] and low-bandgap Sn-based MHPs, [72,73] which serve as essential units in PSCs from single-junctions to tandems. Guided by the revealed mechanisms, we will present examples to highlight the importance of microstructural tailoring to successful implementation in PSCs. We are aware with numerous excellent reviews in the device-oriented research,[74-79] and thus, herein we choose to discuss only a few of the most recent, representative works.

$FAPbI_3$ suffers from a facile polymorphic transition from the semiconducting α phase to a photo-inactive δ phase in the ambient environment, adding to the difficulty in maintaining its structural stability. This detrimental transition is accelerated in the presence of environmental factors such as moisture.[80,81] Herein GBs and surfaces are expected to dominate, as they not only offer paths for the interaction and ingression of moisture into the film bulk, but also create less constrained environment for α-to-δ transition to occur and propagate (**Figure 7a**). Furthermore, the octahedral tilt in the $FAPbI_3$ lattice is found to influence the phase transition.[50] It is tailorable by controlling the IGD density and functionalizing GBs and surfaces, which distorts the lattice internally or externally. Yun *et al*.[23] used AFM to capture the onset of moisture-induced degradation in an $FAPbI_3$ film and confirmed the prominent role of GBs in trapping moisture and triggering polymorphic transition, although it remains unclear how the transition front moves across bulk $FAPbI_3$ grains. These mechanisms understandings have been leveraged to invent state-of-the-art fabrication methods for $FAPbI_3$ PSCs, where rationally selected chemical molecules are used to passivate GBs and surfaces (**Figure 7b**). Jeong *et al*.[11] showed that, by incorporating $HCOO^-$ pseudo-halides in the precursor solution that sequentially interacts with $FAPbI_3$ grain and GBs in the solid film, PSCs with a certified 25.2% PCE and superior device operational stability is achieved (**Figure 7c**), attesting the role of GBs and surface in this degradation mode of phase transition.

Mixed-halide MHPs, widely studied for wide-bandgap top-cells in tandems, undergo light-induced halide segregation, which converts single-phase MHPs into separated I-rich and Br-rich phases and thus lowers V_{OC}.[71] This degradation mode is dominated by ion movement (**Figure 7e**). Therefore, striking phase segregation will occur at where the diffusivity of I and Br differ to the largest extent. Evidence as of now points to GBs as the microstructure type that influence this process mostly. Tang *et al.* [31] monitored time-dependent PL evolutions separately at GB and grain-interior regions. Grain interior is found to retain its intrinsic bandgap emission while red-shifted PL is gradually generated at the GB region, indicative of I-rich domain formation there. Facile halide segregation at GBs may be also related to relaxed strain structures.[82] Therefore, reducing the GB structural dimensionality is an effective mitigation method (**Figure 7f**). Kim *et al*.[83] used PEA(I_xSCN_{1-x}) additive to form 2D second-phases at GBs

of wide-bandgap MHPs (inset of **Figure 7g**). An optimal formation of 2D phases at GBs is achieved by tuning the additive composition, which results in much more stable PSC performance than control devices without or with unoptimized GB tailoring (**Figure 7h**).

For Sn-Pb and Pb-free Sn MHPs, the low oxidation resistance of Sn(II) is a major hurdle, which is subject to its interaction of environmental O_2 species.[84] As illustrated in **Figure 7i**, one possible scenario for the degradation mode will follow two steps: (i) O_2 adsorption by MHP surfaces; (ii) O_2 penetration via GBs that feature a high degree of disorder in their pristine states. Park *et al.*[85] showed the O_2 adsorption energy of pristine $FAPb_{0.5}Sn_{0.5}I_3$ is as low as -1.01 eV, favouring O_2-MHP interaction. Metallic doping can be helpful to increase the O_2 adsorption energy for surfaces and improving the GB disorder, thus enhancing MHP stability. This is consistent with the proposed scenario. Nevertheless, it is challenging to study the atomic-level mechanisms of oxygen-induced degradation of Sn MHPs, because it starts on surfaces that are highly disordered and the relative disordered structure of surfaces limits the studies using local structure characterization methods such as ss-NMR.[86] With regard to devices, multifunctional additives have been used for passivating MHPs surfaces (**Figure 7i)** which address both Sn oxidation and all general processing/stability issues for MHPs.[26,87,88] Lin *et al.*[87] demonstrated zwitterionic antioxidant as a suitable additive which interacts with both Sn and halide vacancies of surface and GBs of mixed Sn-Pb MHP thin films. Zwitterions have also been known as a surfactant that facilitates solution formation of compact grain microstructures. IGDs such as Sn vacancies may also be modulated as their formation can be affected by synthetic conditions. As a result, a stable and efficient perovskite-perovskite tandem device is achieved. Later, Lin *et al.*[89] further studied the absorption stability of passivators on Sn-Pb MHP surfaces, which guides the discovery of 4-trifluoromethyl-phenylammonium cations passivator that leads to a 26.4% certified-PCE perovskite-perovskite tandem with over 600 h T90 operational stability (**Figure 7j)**.

5. Conclusion and Outlook

The past research entailing the use of various characterization techniques have led to significant evidence supporting the outstanding role of MHP microstructures (GBs, IGDs, and surfaces) on the photophysical properties and chemical stability. Meanwhile, the dynamic, coupled interactions of MHP microstructures with photocarriers, intrinsic ions, and extrinsic species/stimuli has offered a fascinating playground for further exploration. Furthermore, the (opto)mechanical properties of PSCs have started to draw attention as interfacial and bulk mechanical degradations can considerably impact the long-term stability in addition to the (photo-)chemical processes.[90] The interplay of cracking with various MHP morphological defects emerges as a new frontier of stability studies in PSCs. All these fundamental energy sciences will be translated for perovskite photovoltaic engineering to create efficient and durable tandems/multijunctions and large-area modules with even more complex MHP microstructures and morphological defects. We briefly propose the following research directions to set solid foundations on the PSC development.

The first is to probe hidden microstructures and underdetermined effects. As mentioned earlier, the relative ease of identifying surface-probed GBs has driven their fundamental understanding matured quickly, which has guided the field to achieve high-performance PSCs from single-junctions to tandems that embrace various MHP compositions. But microstructural details of many essential morphological defects remain hidden, *e.g.* those buried GBs near film bottom surfaces, IGDs characteristics of different types in state-of-the-art MHPs, and these novel device heterointerfaces with high coherence and long-range ordering established in the record-performance PSCs.[58,59,65,91,92,93] In fact, such omission in considering all these hidden/buried features could be one of the causes for the existing discrepancies in the GB roles in PSCs. Therefore, probing hidden microstructures is likely to lead to corrected understandings on established findings. Future studies will urgently call for innovations in materials sample preparation methods and experimental designs to unlock the characterization of these hidden microstructures.

The second is to enable *in-situ*, correlated characterizations and theory-guided interpenetration. Correlated and *in-situ* microscopic studies will be the next key step to decisively understanding microstructure-property-performance relationships in PSCs, since the complex nature of the MHP system introduces tangling factors that are difficult to investigate separately in conventional systematic, macroscopic studies. The development of combinatorial and correlated experimental instrumentation suites are needed to visualize the effect of microstructures on the motion of photocarriers, ions/molecules, as well as cracks in MHPs under controlled conditions. Especially, the recent advances in X-ray and electron microscopies have even demonstrated their excellent capability of in situ (operando) characterization of full (opto)electronic devices, leverageable to probe the structural and functional dynamics in PSCs in real time. In addition, multi-scale theoretical simulations may be further developed to model and statistically capture the observed microstructures structures. Considering the large datasets produced from in-situ, correlated characterizations, machine-learning algorithms will rapidly emerge for interpenetrating the results and guided more targeted exploration.

The third is to harness microstructural imperfections for better PSCs. Earlier we have mainly indicated detrimental roles of many known microstructural imperfections in MHPs. Counterintuitively there could be interesting space for harnessing the potential merits of these imperfections. Taking the example of electronic benign CTBs, it would be intriguing to see whether we can utilize it for tailoring strain in MHPs to enhance the chemical stability. Also, microstructural imperfections may be leveraged for (opto-)mechanical merits. For example, intragrain dislocations in MHPs may be controlled to build more tough interfaces in PSCs. Again, all these will link back to the microscopic structure-property-performance relationship, attesting the significance of this fundamental investigation.

Acknowledgement

Y.Z. acknowledges the start-up grants, the Interdisciplinary Matching Scheme, Initiation Grant - Faculty Niche Research Areas (IG-FNRA) 2020/21 of HKBU, and the Early Career Scheme

(No. 22300221) from the Hong Kong Research Grant Council. L.M.H. acknowledges funding from the Engineering and Physical Sciences Research Council (EPSRC) UK, and support from TUM-IAS through a Hans Fischer Senior Fellowship. A.K.-Y.J. thanks the support from the Lee Shau Kee Chair Professorship and the Innovation and Technology Fund (ITS/497/18FP, GHP/021/18SZ). M.S. acknowledges the German Research Foundation (DFG, GRK 2642, SPP 2196).

Competing interests

The authors declare no competing interests.

Reference

1. Kojima, A., Teshima, K., Shirai, Y. & Miyasaka, T. Organometal halide perovskites as visible-light sensitizers for photovoltaic cells. *J. Am. Chem. Soc.* **131**, 6050-6051 (2009). ***The first report on the use of MHPs for solar cell applications.***
2. Kim, H.-S. *et al.* Lead iodide perovskite sensitized all-solid-state submicron thin film mesoscopic solar cell with efficiency exceeding 9%. *Sci. Rep.* **2**, 591 (2012).
3. Heo, J.H. *et al.* Efficient inorganic-organic hybrid heterojunction solar cells containing perovskite compound and polymeric hole conductors. *Nat. Photon.* **7**, 486-491 (2013).
4. Burschka, J. *et al.* Sequential deposition as a route to high-performance perovskite-sensitized solar cells. *Nature* **499**, 316-319 (2013).
5. Jeon, N.J. *et al.* Solvent engineering for high-performance inorganic–organic hybrid perovskite solar cells. *Nat. Mater.* **13**, 897-903 (2014).
6. Jeon, N.J. *et al.* Compositional engineering of perovskite materials for high-performance solar cells. *Nature* **517**, 476-480 (2015).
7. Yang, W.S. *et al.* High-performance photovoltaic perovskite layers fabricated through intramolecular exchange. *Science* **348**, 1234-1237 (2015).
8. Yang, W.S. *et al.* Iodide management in formamidinium-lead-halide–based perovskite layers for efficient solar cells. *Science* **356**, 1376-1379 (2017).
9. Jung, E.H. *et al.* Efficient, stable and scalable perovskite solar cells using poly (3-hexylthiophene). *Nature* **567**, 511-515 (2019).
10. Jiang, Q. *et al.* Surface passivation of perovskite film for efficient solar cells. *Nat. Photon.* **13**, 460-466 (2019).
11. Jeong, J. *et al.* Pseudo-halide anion engineering for α-$FAPbI_3$ perovskite solar cells. *Nature* **592**, 381-385 (2021).
12. Liu, M., Johnston, M.B. & Snaith, H.J. Efficient planar heterojunction perovskite solar cells by vapour deposition. *Nature* **501**, 395-398 (2013). ***The first report on the use of MHPs in thin film solar cell device configuration.***
13. Min, H. *et al.* Perovskite solar cells with atomically coherent interlayers on SnO_2 electrodes. *Nature* **598**, 444-450 (2021).
14. Green, M.A., Ho-Baillie, A. & Snaith, H.J. The emergence of perovskite solar cells. *Nat. Photon.* **8**, 506-514 (2014).

15. Zhou, Y., Zhou, H., Deng, J., Cha, W. & Cai, Z. Decisive Structural and Functional Characterization of Halide Perovskites with Synchrotron. *Matter* **2**, 360-377 (2020).
16. Zhou, Y., Game, O.S., Pang, S. & Padture, N.P. Microstructures of organometal trihalide perovskites for solar cells: their evolution from solutions and characterization. *J. Phys. Chem. Lett.* **6**, 4827-4839 (2015).
17. Dunlap-Shohl, W.A., Zhou, Y., Padture, N.P. & Mitzi, D.B. Synthetic approaches for halide perovskite thin films. *Chem. Rev.* **119**, 3193-3295 (2018).
18. Dai, Z. *et al.* Interfacial toughening with self-assembled monolayers enhances perovskite solar cell reliability. *Science* **372**, 618-622 (2021).
19. Rothmann, M.U. *et al.* Atomic-scale microstructure of metal halide perovskite. *Science* **370**, eabb5940 (2020). ***The first atomic-scale observation of MHP thin-film microstructures using scanning TEM.***
20. Kim, M.c. *et al.* Advanced characterization techniques for overcoming challenges of perovskite solar cell materials. *Adv. Energy Mater.* **11**, 2001753 (2021).
21. Rothmann, M.U., Li, W., Etheridge, J. & Cheng, Y.B. Microstructural characterisations of perovskite solar cells–from grains to interfaces: Techniques, features, and challenges. *Adv. Energy Mater.* **7**, 1700912 (2017).
22. Li, W. *et al.* Subgrain special boundaries in halide perovskite thin films restrict carrier diffusion. *ACS Energy Lett.* **3**, 2669-2670 (2018).
23. Yun, J.S. *et al.* Humidity-Induced Degradation via Grain Boundaries of $HC(NH_2)_2PbI_3$ Planar Perovskite Solar Cells. *Adv. Funct. Mater.* **28**, 1705363 (2018).
24. Meggiolaro, D., Mosconi, E. & De Angelis, F. Formation of Surface Defects Dominates Ion Migration in Lead-Halide Perovskites. *ACS Energy Lett.* **4**, 779-785 (2019).
25. Zong, Y. *et al.* Continuous grain-boundary functionalization for high-efficiency perovskite solar cells with exceptional stability. *Chem* **4**, 1404-1415 (2018).
26. Zong, Y., Zhou, Z., Chen, M., Padture, N.P. & Zhou, Y. Lewis-Adduct Mediated Grain-Boundary Functionalization for Efficient Ideal-Bandgap Perovskite Solar Cells with Superior Stability. *Adv. Energy Mater.* **8**, 1800997 (2018).
27. Jiang, J. *et al.* Carrier lifetime enhancement in halide perovskite via remote epitaxy. *Nat. Commun.* **10**, 4145 (2019).
28. Xiao, X. *et al.* Benign ferroelastic twin boundaries in halide perovskites for charge carrier transport and recombination. *Nat. Commun.* **11**, 2215 (2020).
29. Stecker, C. *et al.* Surface Defect Dynamics in Organic–Inorganic Hybrid Perovskites: From Mechanism to Interfacial Properties. *ACS Nano* **13**, 12127-12136 (2019).
30. Li, F. *et al.* Regulating Surface Termination for Efficient Inverted Perovskite Solar Cells with Greater Than 23% Efficiency. *J. Am. Chem. Soc.* **142**, 20134-20142 (2020).
31. Tang, X. *et al.* Local Observation of Phase Segregation in Mixed-Halide Perovskite. *Nano Lett.* **18**, 2172-2178 (2018).
32. Zheng, G. *et al.* Manipulation of facet orientation in hybrid perovskite polycrystalline films by cation cascade. *Nat. Commun.* **9**, 2793 (2018).
33. Leblebici, S.Y. *et al.* Facet-dependent photovoltaic efficiency variations in single grains of hybrid halide perovskite. *Nat. Energy* **1**, 16093 (2016). ***An early study on the heterogenous photovoltaic response on the surface of MHP thin films.***

34. Khanna, R. & Sahajwalla, V. Chapter 2.3 - Atomistic Simulations of Properties and Phenomena at High Temperatures. in *Treatise on Process Metallurgy* (ed. Seetharaman, S.) 287-393 (Elsevier, Boston, 2014).
35. Tennyson, E.M., Doherty, T.A.S. & Stranks, S.D. Heterogeneity at multiple length scales in halide perovskite semiconductors. *Nat. Rev. Mater.* **4**, 573-587 (2019).
36. Banerjee, S. & Saha, H. Grain Boundary effects in polycrystalline silicon solar cells. *Sol. Cells* **28**, 77-94 (1990).
37. Tritscher, P. & Broadbridge, P. Grain boundary grooving by surface diffusion: an analytic nonlinear model for a symmetric groove. *Proc. R. Soc. Lond. A* **450**, 569-587 (1995).
38. Zhou, Y., Sternlicht, H. & Padture, N.P. Transmission electron microscopy of halide perovskite materials and devices. *Joule* **3**, 641-661 (2019).
39. Cai, S. *et al.* Atomically Resolved Electrically Active Intragrain Interfaces in Perovskite Semiconductors. *J. Am. Chem. Soc.* **144**, 1910-1920 (2022). ***The first study imaging the atomic-scale microstructure of IGDs in PSCs.***
40. Song, J., Zhou, Y., Padture, N.P. & Huey, B.D. Anomalous 3D nanoscale photoconduction in hybrid perovskite semiconductors revealed by tomographic atomic force microscopy. *Nat. Commun.* **11**, 3308 (2020). ***The first 3D imaging of grain boundary networks in MHP thin films.***
41. Ercius, P., Alaidi, O., Rames, M.J. & Ren, G. Electron Tomography: A Three-Dimensional Analytic Tool for Hard and Soft Materials Research. *Adv. Mater.* **27**, 5638-5663 (2015).
42. Shao, Y. *et al.* Grain boundary dominated ion migration in polycrystalline organic–inorganic halide perovskite films. *Energy Environ. Sci.* **9**, 1752-1759 (2016).
43. Jariwala, S. *et al.* Local Crystal Misorientation Influences Non-radiative Recombination in Halide Perovskites. *Joule* **3**, 3048-3060 (2019).
44. Rothmann, M.U. *et al.* Direct observation of intrinsic twin domains in tetragonal $CH_3NH_3PbI_3$. *Nat. Commun.* **8**, 14547 (2017). Note: *The first microscopic observation of twin domains in MHP thin films.*
45. Thind, A.S. *et al.* Atomic Structure and Electrical Activity of Grain Boundaries and Ruddlesden–Popper Faults in Cesium Lead Bromide Perovskite. *Adv. Mater.* **31**, 1805047 (2019).
46. Cheng, S.Y., Ho, N.J. & Lu, H.Y. Transformation-Induced Twinning: The 90° and 180° Ferroelectric Domains in Tetragonal Barium Titanate. *J. Am. Chem. Soc.* **89**, 2177-2187 (2006).
47. Li, W. *et al.* The critical role of composition-dependent intragrain planar defects in the performance of $MA_{1-x}FA_xPbI_3$ perovskite solar cells. *Nat. Energy* **6**, 624–632 (2021). ***The first systematic study on the relationship between IGDs characteristics and MHP properties and performance.***
48. Reiche, M. *et al.* On the electronic properties of a single dislocation. *J. Appl. Phys.* **115**, 194303 (2014).
49. Xue, J., Wang, R. & Yang, Y. The surface of halide perovskites from nano to bulk. *Nat. Rev. Mater.* **5**, 809-827 (2020).

50. Doherty, T.A.S. *et al.* Stabilized tilted-octahedra halide perovskites inhibit local formation of performance-limiting phases. *Science* **374**, 1598-1605 (2021).
51. Li, N., Niu, X., Chen, Q. & Zhou, H. Towards commercialization: the operational stability of perovskite solar cells. *Chem. Soc. Rev.* **49**, 8235-8286 (2020).
52. Kong, J. *et al.* CO_2 doping of organic interlayers for perovskite solar cells. *Nature* **594**, 51-56 (2021).
53. Kubicki, D.J., Stranks, S.D., Grey, C.P. & Emsley, L. NMR spectroscopy probes microstructure, dynamics and doping of metal halide perovskites. *Nat. Rev. Chem.* **5**, 624–645 (2021).
54. Dahlman, C.J., Kubicki, D.J. & Reddy, G.N.M. Interfaces in metal halide perovskites probed by solid-state NMR spectroscopy. *J. Mater. Chem. A* **9**, 19206-19244 (2021).
55. Chen, Y. *et al.* Surface termination of $CsPbBr_3$ perovskite quantum dots determined by solid-state NMR spectroscopy. *J. Am. Chem. Soc.* **142**, 6117-6127 (2020).
56. Yuan, J., Bao, H., Liu, H., Wang, S. & Li, X. Mixed solvent atmosphere induces the surface termination state transition of perovskite to achieve matched energy level alignment. *Chem. Eng. J.* **424**, 130508 (2021).
57. Liu, Y. *et al.* Atomistic Origins of Surface Defects in $CH_3NH_3PbBr_3$ Perovskite and Their Electronic Structures. *ACS Nano* **11**, 2060-2065 (2017).
58. Azmi, R. *et al.* Damp heat-stable perovskite solar cells with tailored-dimensionality 2D/3D heterojunctions. *Science* **376**, 73-77 (2022).
59. Chen, H. *et al.* Quantum-size-tuned heterostructures enable efficient and stable inverted perovskite solar cells. *Nat. Photon.* (2022).
60. de Quilettes, D.W. *et al.* Impact of microstructure on local carrier lifetime in perovskite solar cells. *Science* **348**, 683-686 (2015). ***The first microstructure-property correlated study revealing the detrimental effects of GBs in MHPs.***
61. Li, W. *et al.* Direct characterization of carrier diffusion in halide-perovskite thin films using transient photoluminescence imaging. *ACS Photonics* **6**, 2375-2380 (2019).
62. Yun, J.S. *et al.* Benefit of Grain Boundaries in Organic–Inorganic Halide Planar Perovskite Solar Cells. *J. Phys. Chem. Lett.* **6**, 875-880 (2015).
63. Chu, Z. *et al.* Impact of grain boundaries on efficiency and stability of organic-inorganic trihalide perovskites. *Nat. Commun.* **8**, 2230 (2017).
64. Pham, H.T., Duong, T., Weber, K.J. & Wong-Leung, J. Insights into Twinning Formation in Cubic and Tetragonal Multi-cation Mixed-Halide Perovskite. *ACS Mater. Lett.* **2**, 415-424 (2020).
65. Tan, S. *et al.* Stability-limiting heterointerfaces of perovskite photovoltaics. *Nature* (2022). Note: *The first study mechanistically revealing the negative impact of regular passivation strategies on the stablity of heterointerfaces in PSCs.*
66. Juarez-Perez, E.J. *et al.* Photodecomposition and thermal decomposition in methylammonium halide lead perovskites and inferred design principles to increase photovoltaic device stability. *J. Mater. Chem. A* **6**, 9604-9612 (2018).
67. Wang, Q. *et al.* Scaling behavior of moisture-induced grain degradation in polycrystalline hybrid perovskite thin films. *Energy Environ. Sci.* **10**, 516-522 (2017).
68. Alberti, A. *et al.* Pb clustering and PbI_2 nanofragmentation during methylammonium lead iodide perovskite degradation. *Nat. Commun.* **10**, 2196 (2019).

69. Ju, M.-G. *et al.* Toward eco-friendly and stable perovskite materials for photovoltaics. *Joule* **2**, 1231-1241 (2018).
70. Eperon, G.E. *et al.* Formamidinium lead trihalide: a broadly tunable perovskite for efficient planar heterojunction solar cells. *Energy Environ. Sci.* **7**, 982-988 (2014).
71. Knight, A.J. & Herz, L.M. Preventing phase segregation in mixed-halide perovskites: a perspective. *Energy Environ. Sci.* **13**, 2024-2046 (2020).
72. Awais, M., Kirsch, R.L., Yeddu, V. & Saidaminov, M.I. Tin Halide Perovskites Going Forward: Frost Diagrams Offer Hints. *ACS Mater. Lett.* **3**, 299-307 (2021).
73. Hu, M. *et al.* Sub-1.4eV bandgap inorganic perovskite solar cells with long-term stability. *Nat. Commun.* **11**, 151 (2020).
74. Jena, A.K., Kulkarni, A. & Miyasaka, T. Halide Perovskite Photovoltaics: Background, Status, and Future Prospects. *Chem. Rev.* **119**, 3036-3103 (2019).
75. Wang, R. *et al.* Prospects for metal halide perovskite-based tandem solar cells. *Nat. Photon.* **15**, 411-425 (2021).
76. Cao, J. & Yan, F. Recent progress in tin-based perovskite solar cells. *Energy Environ. Sci.* **14**, 1286-1325 (2021).
77. Zhang, F. *et al.* Advances in two-dimensional organic–inorganic hybrid perovskites. *Energy Environ. Sci.* **13**, 1154-1186 (2020).
78. Li, H. & Zhang, W. Perovskite Tandem Solar Cells: From Fundamentals to Commercial Deployment. *Chem. Rev.* **120**, 9835-9950 (2020).
79. Zhou, Y., Poli, I., Meggiolaro, D., De Angelis, F. & Petrozza, A. Defect activity in metal halide perovskites with wide and narrow bandgap. *Nat. Rev. Mater.* **6**, 986–1002 (2021).
80. Zhou, Y., Yang, M., Pang, S., Zhu, K. & Padture, N.P. Exceptional Morphology-Preserving Evolution of Formamidinium Lead Triiodide Perovskite Thin Films via Organic-Cation Displacement. *J. Am. Chem. Soc.* **138**, 5535-8 (2016).
81. Wang, Z. *et al.* Additive-Modulated Evolution of $HC(NH_2)_2PbI_3$ Black Polymorph for Mesoscopic Perovskite Solar Cells. *Chem. Mater.* **27**, 7149-7155 (2015).
82. Chen, Z., Brocks, G., Tao, S. & Bobbert, P.A. Unified theory for light-induced halide segregation in mixed halide perovskites. *Nat.Commun.* **12**, 2687 (2021).
83. Kim, D. *et al.* Efficient, stable silicon tandem cells enabled by anion-engineered wide-bandgap perovskites. *Science* **368**, 155-160 (2020).
84. Jiang, X. *et al.* Tin Halide Perovskite Solar Cells: An Emerging Thin-Film Photovoltaic Technology. *Acc. Mater. Res.* **2**, 210-219 (2021).
85. Park, C., Choi, J., Min, J. & Cho, K. Suppression of Oxidative Degradation of Tin–Lead Hybrid Organometal Halide Perovskite Solar Cells by Ag Doping. *ACS Energy Lett.* **5**, 3285-3294 (2020).
86. Kubicki, D.J. *et al.* Local Structure and Dynamics in Methylammonium, Formamidinium, and Cesium Tin(II) Mixed-Halide Perovskites from 119Sn Solid-State NMR. *J. Am. Chem. Soc.* **142**, 7813-7826 (2020).
87. Lin, R. *et al.* Monolithic all-perovskite tandem solar cells with 24.8% efficiency exploiting comproportionation to suppress Sn (II) oxidation in precursor ink. *Nat. Energy* **4**, 864-873 (2019).

88. Liu, X. *et al.* Efficient and stable tin perovskite solar cells enabled by amorphous-polycrystalline structure. *Nat. Commun.* **11**, 2678 (2020).
89. Lin, R. *et al.* All-perovskite tandem solar cells with improved grain surface passivation. *Nature* **603**, 73-78 (2022).
90. Dai. Z. *et al.* Interfacial toughening with self-assembled monolayers enhances perovskite solar cell reliability. *Science* **372**, 618-622 (2021).
91. Kim, M. *et al.* Conformal quantum dot-SnO_2 layers as electron transporters for efficient perovskite solar cells. *Science* **375**, 302-306 (2022).
92. Li, X. *et al.* Constructing heterojunctions by surface sulfidation for efficient inverted perovskite solar cells. *Science* **375**, 434-437 (2022).
93. Dong, Q. *et al.* Interpenetrating interfaces for efficient perovskite solar cells with high operational stability and mechanical robustness. *Nat. Commun.* **12**, 973 (2021).

Figures and Box

Box 1. Evolution of the perovskite microstructure along the technological progression of solar cells.

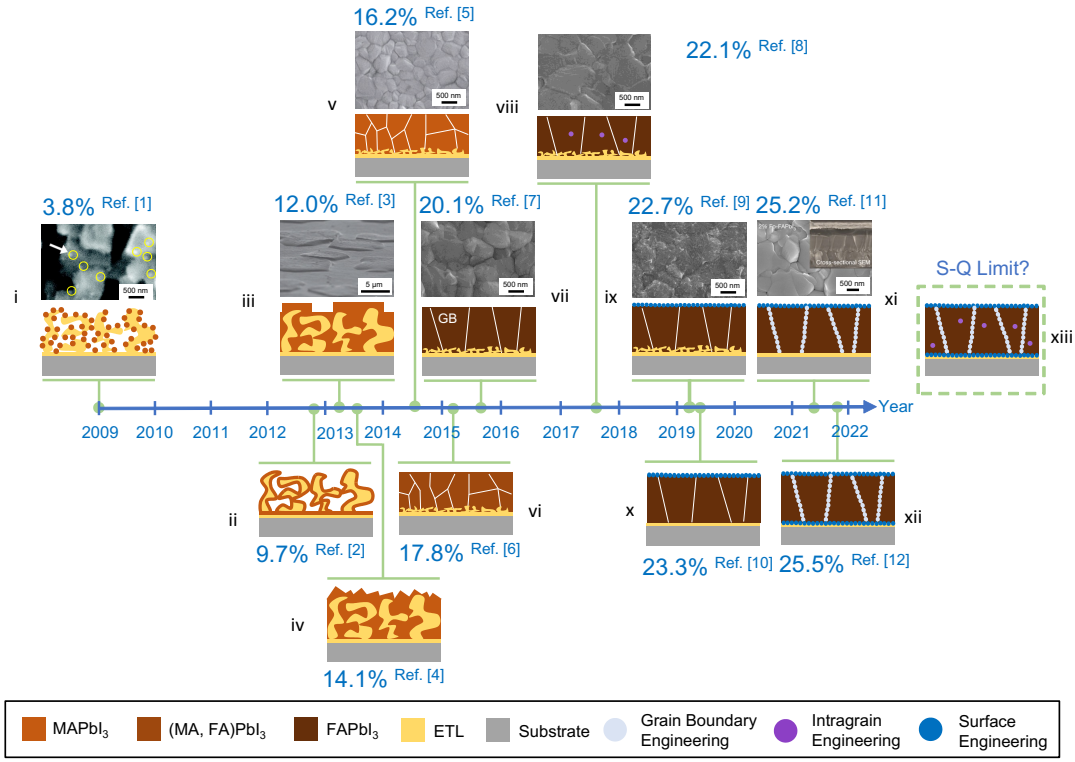

Figure B1. Roadmap showing the PCE evolution of PSCs over time, and representative MHP films and device microstructures in corresponding PSCs. The detailed structure of each device upon the evolution is elaborated in **Box 1**. Sketches in the regions (i-xiii) illustrate the essential PSC structures (omitting HTLs and top contacts) from cross-section views. SEM images in the regions (i-xi) show top-view microstructures of the MHP films in corresponding devices, except that in (iii) is viewed with slight tilting. SEM image in (xii) is also top-view with the inset showing cross-section. SEM images (**c**) are adapted from ref. [1] with permission from the American Chemical Society, ref. [2] under the Creative Commons license, ref. [3,5,9,11] with permission from the Springer Nature, and ref. [7,8] with permission from the American Association for the Advancement of Science (AAAS).

Figure B1 displays a roadmap showing the evolution of MHP film and device microstructures in record-PCE PSCs over time, which reveals three characteristic development periods for the PSC technology. This first period (2009-2014) demonstrates the effort improving the absorber films of $MAPbI_3$ MHPs to a smooth, compact, polycrystalline microstructure, which led to the steepest increase of PCE from 3.8% to 16.1%. The second period (2014-2015) mainly features a composition transition of MHPs ($MAPbI_3$ to $FAPbI_3$) to extend the light absorption while

maintaining the compact polycrystalline film microstructure. In the latest period (2015 to now), effort has been devoted to nanoscale or even atomic-scale modification of GBs, intragrain defects (IGDs), and surface/interface microstructures in the $FAPbI_3$-based MHP thin films. Specifically, the region (i) shows the first version of PSC with $MAPbI_3$ MHP fabricated in a discontinuous, quantum-dot morphology and deposited on mesoporous TiO_2 ETL.[1] The region (ii) illustrates a later version with perovskite forming a continuous, nanoscale thin layer on mesoporous TiO_2 ETL.[2] The region (iii) shows the PSC with $MAPbI_3$ MHP filling the mesoporous TiO_2 ETL and forming a pillared capping layer,[3] and the uniformity of such capping $MAPbI_3$ MHP layer was then improved by the adoption of so-called sequential deposition, leading to a PSC structure as shown in region (iv).[4] In the region (v), solvent engineering is invented for the $MAPbI_3$ MHP fabrication, creating a compact, polycrystalline film morphology.[5] The following studies are devoted to achieve near-pure $FAPbI_3$ composition to extend the light absorption while creating compact films with reduced GB density, successively leading to the device structures as shown in the region (vi-vii).[6,7] This record was then topped with a protocol that enable the manipulation of the internal iodine vacancies in $FAPbI_3$ thin films as seen in the region (viii).[8] In the nearest years, PCE advances have been led by the passivation of $FAPbI_3$ MHP top surface using different 2D phases, as shown in the region (ix-x),[9,10] and simultaneous passivation of both top surface and GBs using pseudo-halide additive,[11] as shown in the region (xi). A certified 25.5 % PCE is achieved via atomic-scale engineering of coherent interfaces between the buried $FAPbI_3$ MHP surface with the SnO_2 ETL, as shown in region (xii).[12] An optimal PSC may be created in the future that simultaneously optimizes GBs, IGDs, and surfaces, which may lead to stable PCEs approaching to Shockley-Queisser limit, as shown in region (xiii). The evolution of detailed PSC structures reflects the urgency in tailoring GB, IGD, and surface microstructures in more targeted and precise manner, because such enhanced microstructures can potentially mitigate detrimental effects, as well as harnessing any potential merits, on the electronic transport and ionic/phase stability of MHPs and PSCs.

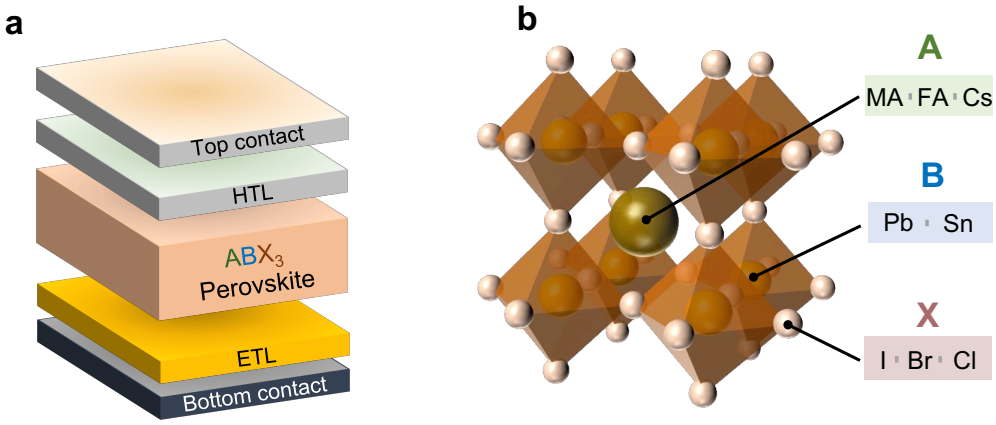

Figure 1. Description and progress of perovskite solar cells. (**a**) Schematics showing the layer-by-layer device structure of a typical PSC. HTL and ETL refer to hole-transporting and electron-transport layer, respectively. (**b**) Schematic structure of the MHP semiconductor family (chemical formula: ABX_3) most typically implemented in PSCs.

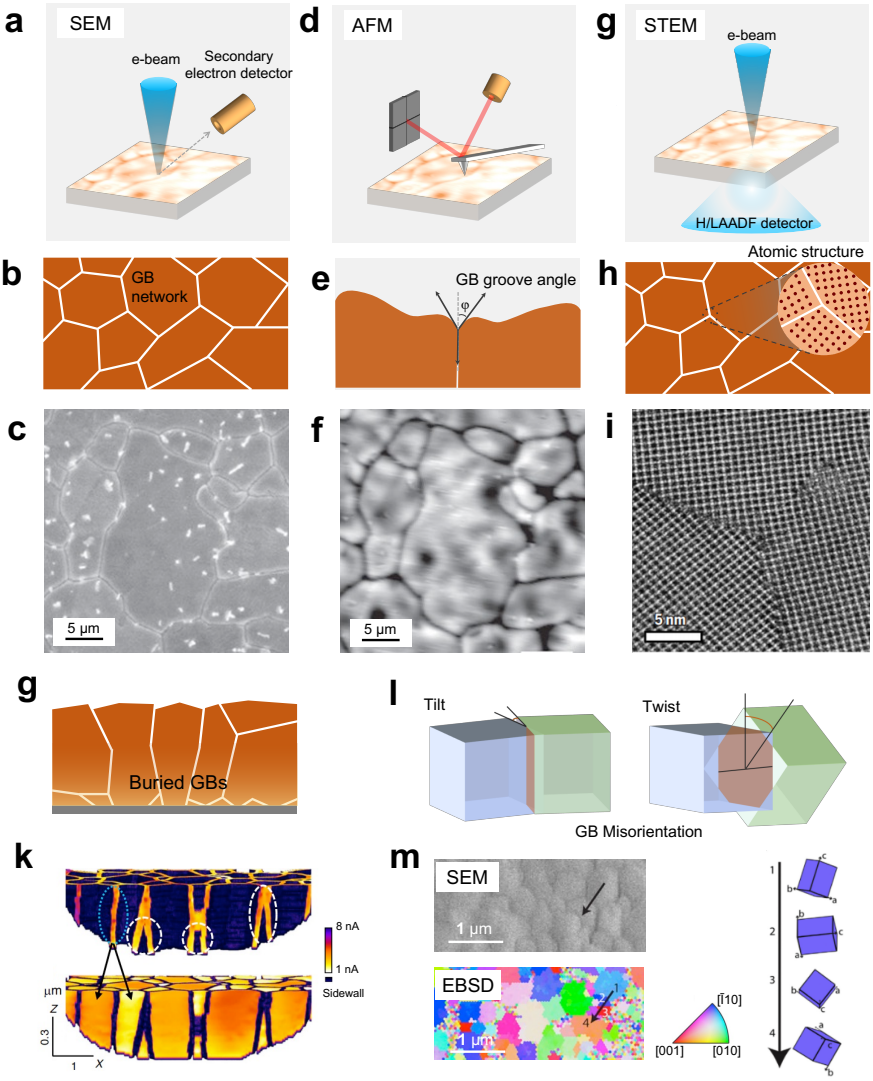

Figure 2. Morphological characteristics of MHP GBs. (**a-c**) GB characterization using SEM: (**a**) schematics of SEM method; (**b**) schematics of GB density characteristics measurable using SEM; (**c**) a typical SEM image (top-view) of an $FAPbI_3$ MHP film. (**d-f**) GB characterization using AFM: (**d**) schematics of AFM method; (**e**) schematics (cross-section) of GB groove angle characteristics determinable using AFM; (**f**) a typical AFM topographic image of an $FAPbI_3$ MHP film. (**g-i**) GB characterization using SEM: (**g**) schematics of STEM method; (**h**) schematics of atomic-scale GB characteristics (plan-view) measurable using STEM; The inset is a zooming-in display illustrating the atomic structure of a GB. (**i**) a typical STEM image of an $FAPbI_3$ MHP film. (**j-k**) Buried GBs in MHPs: (**j**) schematic illustration; (**k**) Segmented cross-sectional tomograms of GBs (top) and grain interiors (bottom), revealing GBs visible at and buried underneath the film surface, respectively. The images are acquired based on the tomographic (conductive) AFM characterization. Blue dash and white dash circles denote the visible and buried GB, respectively. The colour bar shows the scale of current under this AFM measurement. Sidewall in top and bottom panels refers to grain interior and GB, respectively. (**l-m**) GB misorentation: (**l**) Schematics showing two types of GB misorientation; The blue and green colours represent grains with different grains. (**m**)

Demonstration of GB misorentation measurements using correlated SEM (left top) and EBSD (inverse pole figure map; left bottom) for an $MAPbI_3$ MHP thin film. The colour bar is the index map for the crystal planes of the film surface. The 001 (in bold) in the IPF color key indicates that the IPF map plotted is along the sample z direction. The black arrow in the SEM and EBSD images shows a typical transition of grain orientation across four grains (donated as 1, 2, 3, 4) and three GBs. On the right panel, depiction of changes in local crystal orientation along the black arrow is shown as viewed normal to the sample. (**c, f**) are adopted from ref. [22] from the American Chemical Society. (**i**) is adopted from ref. [19] with permission from the American Association for the Advancement of Science (AAAS). (**k**) is adapted from ref. [40] under the Creative Commons license. (**m**) is adopted from ref. [43] with the permission from Elsevier.

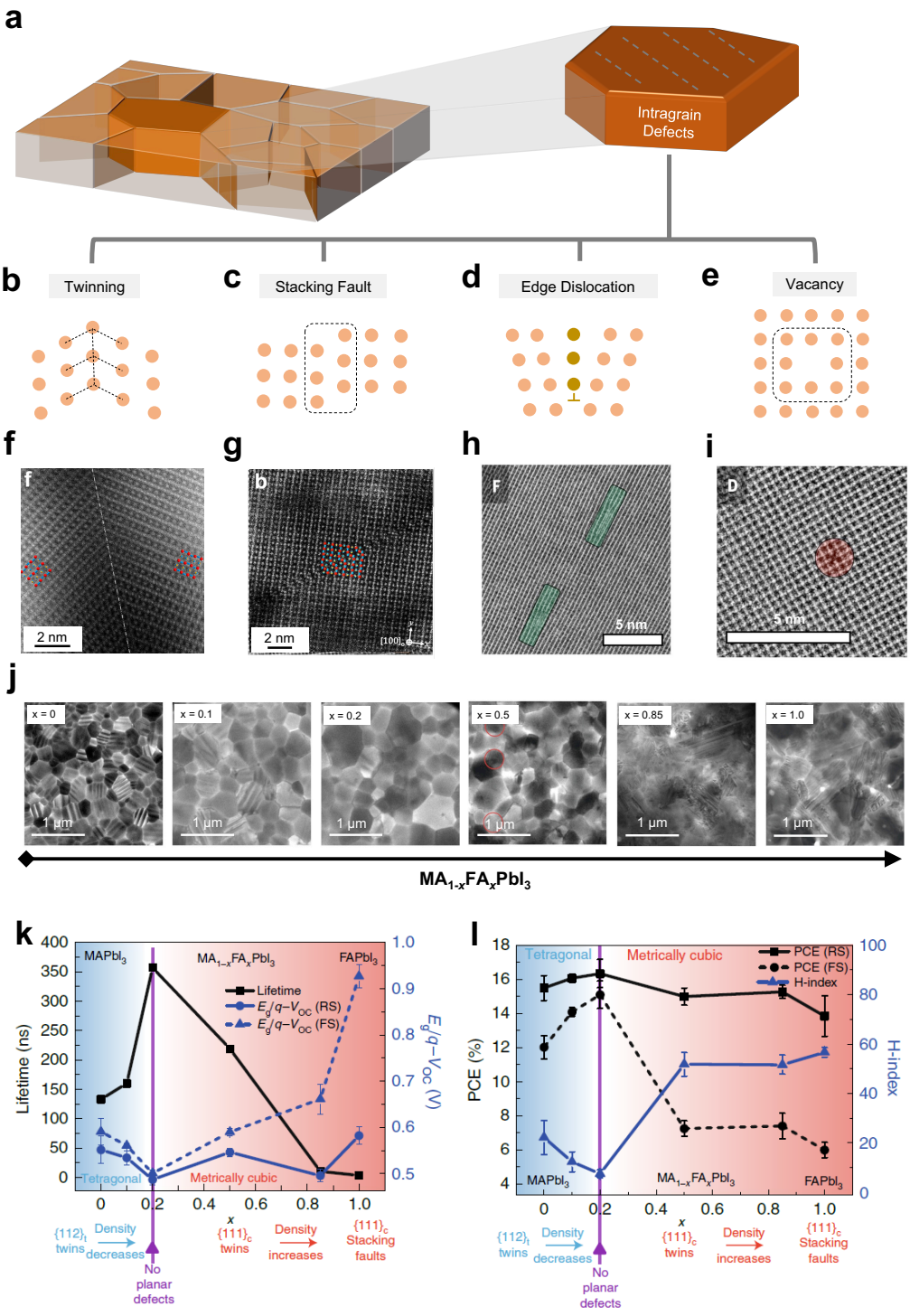

Figure 3. Morphological characteristics of MHP IGDs. (a-e) Schematics showing various types of IGDs existing in MHP single grains: (**a**) overall proliferation of IGDs (illustrated using grey dash lines). (**b**) CTB; (**c**) SF; (**d**) dislocation; (**e**) vacancy. (**f-i**) atomic-resolution STEM images of IGDs: (**f**) CTB; (**g**) SF; (**h**) dislocation; (**i**) vacancy. The labelled/highlighted regions in (**g-i**) shows the presence of CTBs, SFs, edge dislocations, and vacancy defects. (**j-l**) composition-dependent IGDs distributions: (**j**) low-magnification TEM images of $MA_{1-x}FA_xPbI_3$ MHPs (x = 0-1); (**k**-l) Analysis of the systematic relationship amongst the MHP composition, IGD characteristics, carrier lifetime,

and device parameters. (**f-g**) is adopted from ref. [39] with the permission under the Creative Commons licence; (**h-i**) is adapted from ref. [19] from the American Association for the Advancement of Science (AAAS); (j-l) is adopted from ref. [47] the permission under the Creative Commons licence.

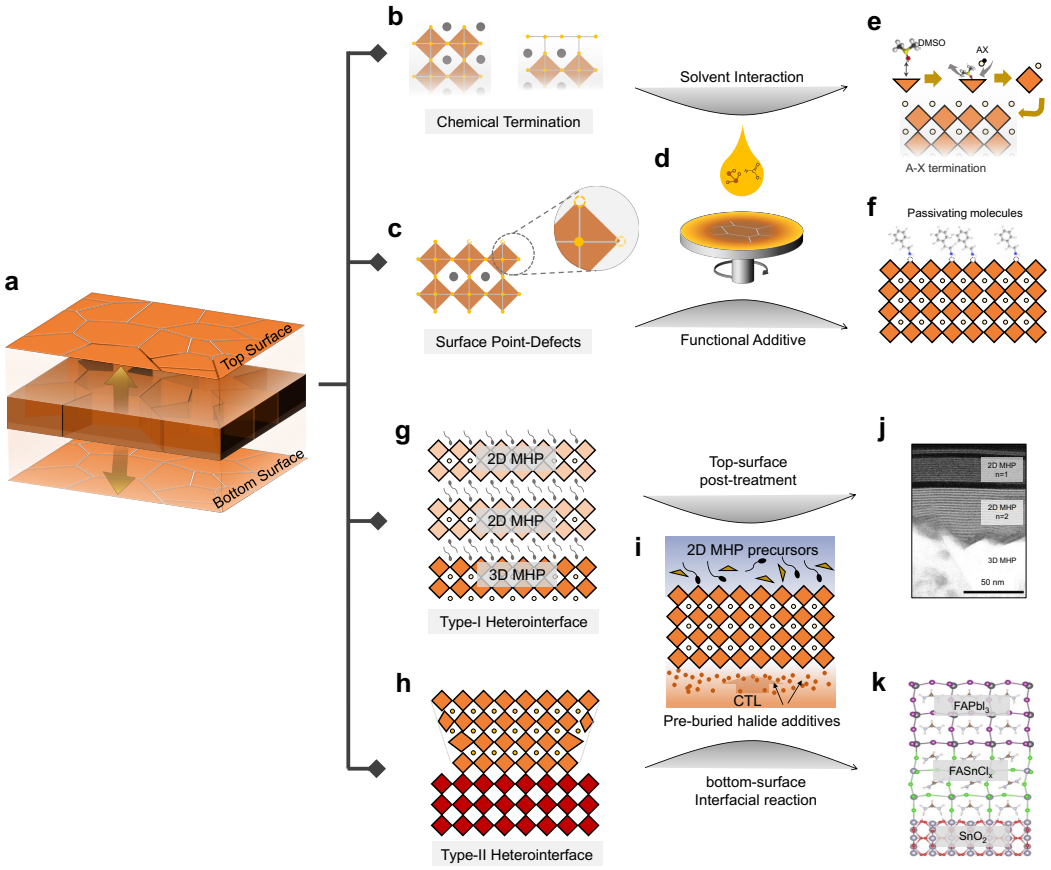

Figure 4. Morphological characteristics of MHP Surfaces. (a) Schematic illustration of MHP surfaces in an MHP film. **(b-f)** Illustration of intrinsic surface characteristics: (**b**) chemical termination; (**c**) surface point-defects; The zoomed-in sketch illustrates an example of halide vacancies on a perovskite octahedral. (**d**) generic method for tailoring chemical termination and surface point-defects via solution chemistry control; (**e**) representative example using solvent chemistry to tailor chemical termination; (**f**) representative example using PEAI additive to passivate surface point-defects. (**g-k**) Illustration of heterointerface characteristics: (**g**) type-I heterointerface formed between 3D MHP and lattice-matched 2D MHP; (**h**) type II heterointerface formed between 3D MHPs of different compositions (illustrated in orange and red colours) with lattice-mismatch-induced interfacial strain; The irregular quadrilaterals represent distorted perovskite octahedra due to the interfacial strain. (**i**) generic method for forming type-I and type-II heterointerfaces via interfacial reaction induced by pre-buried additive and surface post-treatment, respectively. (**j**) representative example showing a type-I heterointerface of 3D MHP with 2D MHP top layer. (**k**) representative example showing the TEM image of a type-II heterointerface of

$FAPbI_3/FASnCl_x$ on SnO_2 ETL. (**e**) is based on ref. [56] with permission from the American Association for the Advancement of Science (AAAS); (**e, g, i, k**) are based on ref. [10,13,59] with permission from the Springer-Nature. (**j**) is adapted from ref. [58] from the American Association for the Advancement of Science (AAAS).

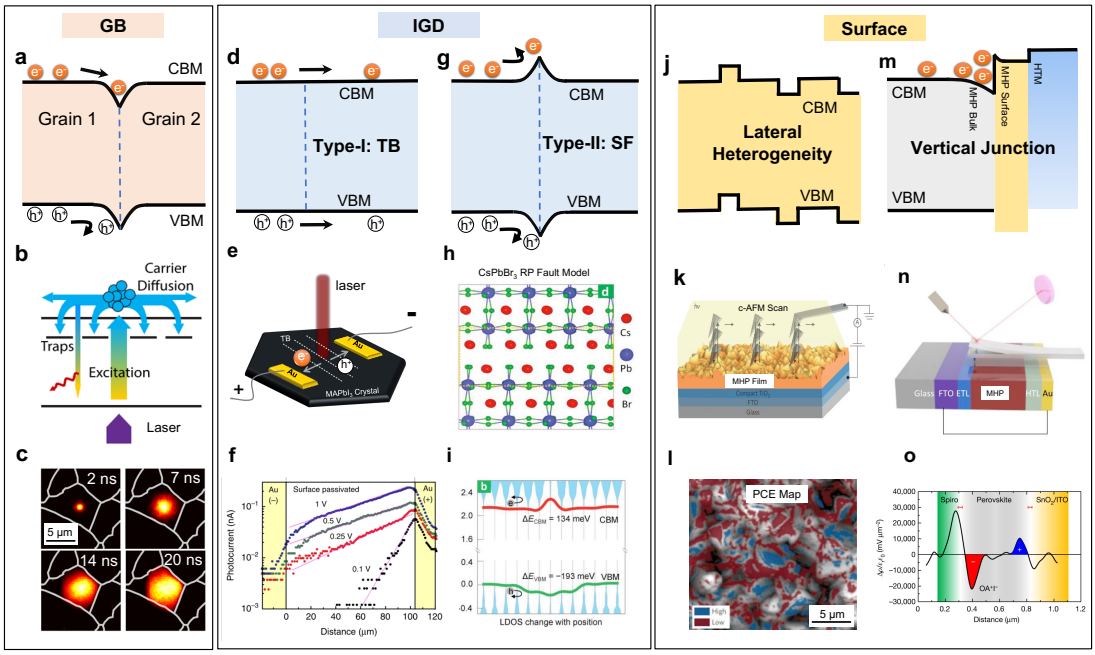

Figure 5. Photophysical Properties of MHP GBs, IGDs, and surfaces. (**a-c**) GB: (**a**) Schematic energy diagram at GB showing a downward band bending; (**b**) Schematic illustration of wide-field transient PL imaging method for in-situ visualization of photocarrier diffusion in MHP thin films; (**c**) Real-time image showing the blocking of photocarrier diffusion at GBs observed using the method in (**b**). (**d-i**) IGD: (**d**) Schematic energy diagram at CTBs showing no band bending; (**e**) Schematic illustration showing the experimental setup of scanning photocurrent microscope for determining carrier transport at CTBs within a GB-free $MAPbI_3$ crystal; (**f**) Photocurrent profiles (under various electric biases) across the conductive channel within the GB-free $MAPbI_3$ crystal using the setup in (f); (**g**) Schematic energy diagram at a stacking fault (SF) showing a downward bending of VBM and an upward bending of CBM; (**h**) crystal model of a SF equivalent to the atomic-scale structure from STEM observation; (**i**) Layer-by-layer projection of DOS and bandgap diagram. (**j-o**) Surface: (**j**) Schematic illustration showing the lateral profile of MHP surface electronic structure; (**k**) conductive AFM measurement on the MHP thin film in the PSC device setting. (**l**) PCE mapping converted from the J_{SC} and V_{OC} mappings using the setup in (**k**); (**m**) Schematic illustration showing the vertical profile of MHP surface electronic structure; (**n**) KPFM surface potential mapping based on FIBed PSC cross-section for studying the vertical energetics of MHP surfaces. (**o**) OAI-treated PSC cross-sections measured by cross-sectional KPFM, indicating the surface accumulation of electrons. (**b-c**) is adapted from ref. [65] with permission from the American Chemical Society. (**f-g**) is adapted or modified from ref. [33] under the Creative Commons licence. (**i-j**) is adapted from ref. [48] with permission from the Wiley. (**m, o**) is adapted from ref.

[65] with permission from the Springer-Nature. (**n**) is adapted from ref. [33] under the Creative Commons licence.

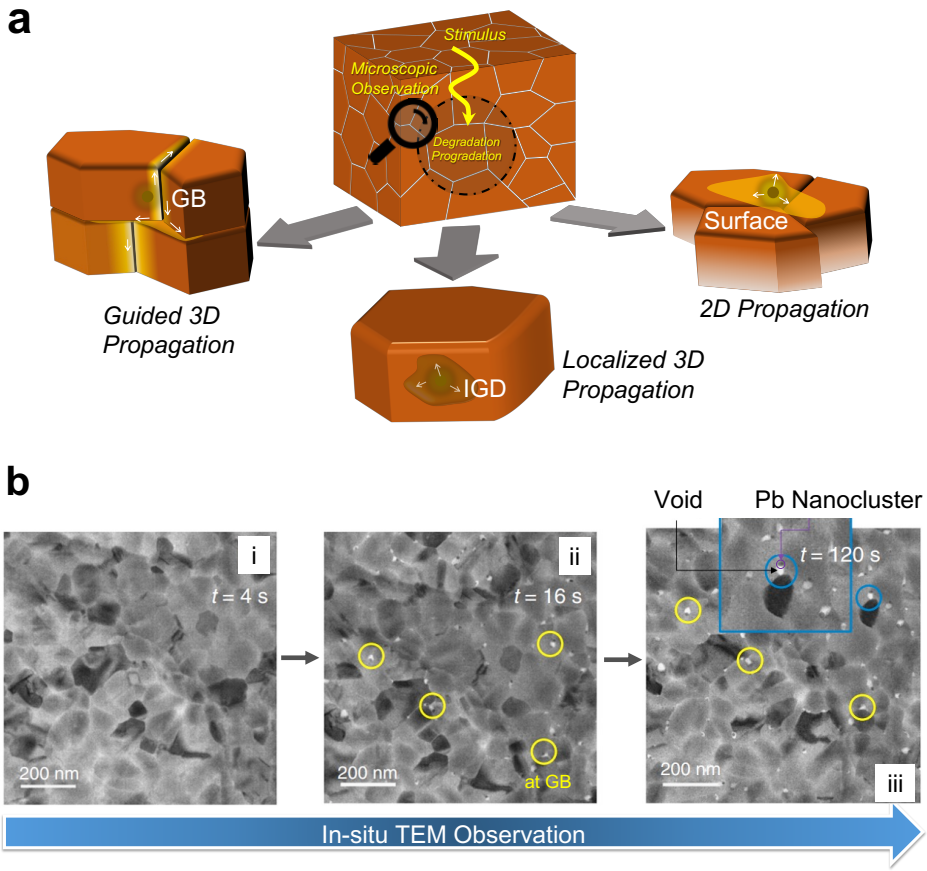

Figure 6. Propagation modes of phase degradation processes at different microstructural features of MHPs. (a) Schematic illustrations of propagation pathways for degradation occurring at GBs, IGDs, and surface. The centre subfigure illustrates the methodology for studying the microstructure-dependent degradation dynamics using *in-situ* microscopic observation. The while arrows in the other three subfigures represents the progradation direction and the dark spot indicates the location where the degradation initializes. **(b)** Example demonstrating an In-situ TEM approach to reveal $MAPbI_3$ MHP degradation propagation under electron beam irradiation is Pb clustering at GBs: images labelled as (i-iii) shows the top-view grain and GB microstructures upon irradiation at different times (4 s, 16 s, and 120 s). Typical GB regions are highlighted using open circles. The inset of image (iii) shows a zoomed-in observation featuring the coexistence of a void and a Pb nanocluster. (**b**) is adapted from ref. [71] with the permission under the Creative Commons licence.

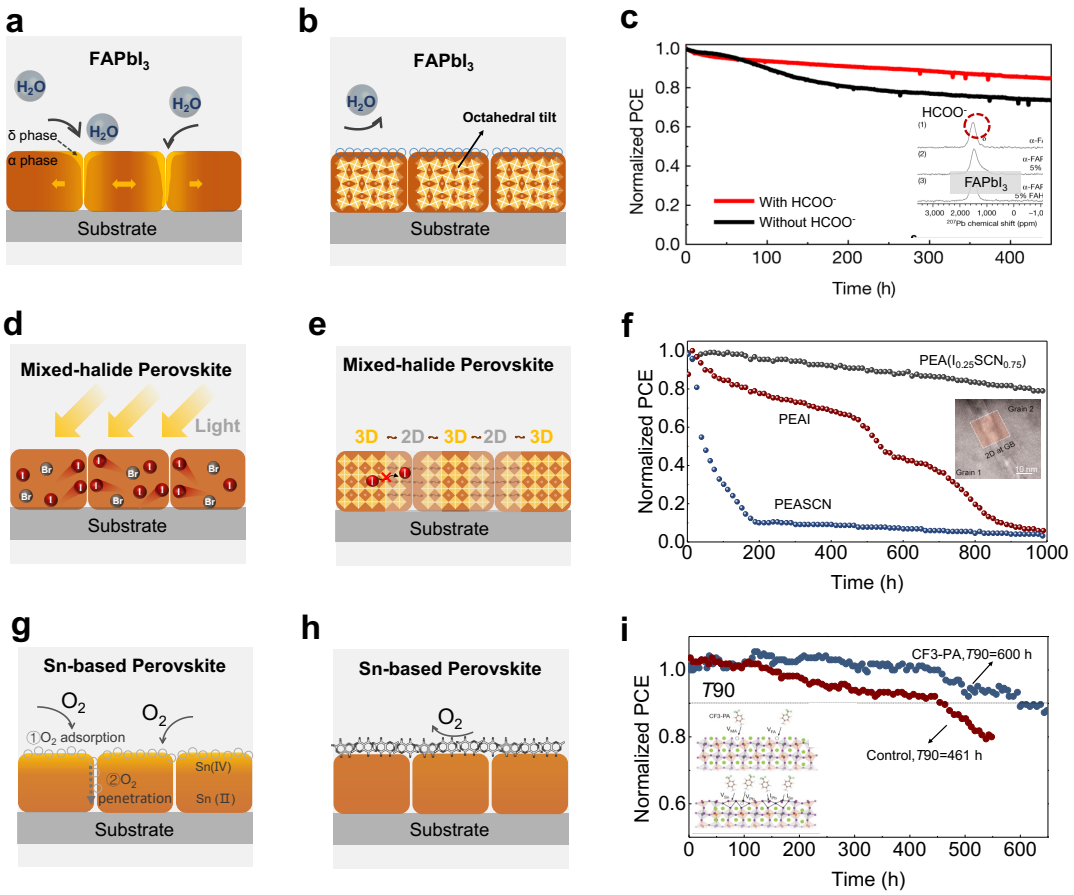

Figure 7. Composition-dependent degradation modes of MHPs and impacts on state-of-the-art PSC development. (a-c) $FAPbI_3$ MHPs: (**a**) Schematic illustration showing moisture-induced degradation of an $FAPbI_3$ film based on phase transformation, featuring the moisture trapping at GBs and correspondingly accelerated propagation of α→δ phase transformation; (**b**) Schematic illustration showing a generic method to stabilize $FAPbI_3$ MHPs entailing GB and surface functionalization that either repel moisture or tilts the octahedral in the lattice; (**c**) Operational stability of a state-of-the-art $FAPbI_3$ PSC made via pseudo-halide passivation as compared to that of a normal device. Inset is schematic illustrating anchoring of $HCOO^-$ pseudo-halide anions on $FAPbI_3$ surface lattice. **(d-f)** Mixed-halide MHPs: (**d**) Schematic illustration showing photo-induced degradation based on halide segregation, featuring the iodine aggregation at GBs; (**e**) Schematic illustration showing a generic method to stabilize mixed-halide MHPs entailing constructing low-dimensional GBs to retard the halide segregation. (**g**) Operational stabilities of wide-bandgap $FA_{0.65}MA_{0.2}Cs_{0.15}PbI_{2.4}Br_{0.6}$ PSCs fabricated by GB engineering with tailored $PEA(I_{0.25}SCN_{0.75})$ 2D phase, pure PEAI, and PEASCN. Inset is cross-sectional TEM of the PSC with GB engineering using 2D phases; **(g-i)** Sn-based MHPs: (**g**) schematic illustration showing oxygen-induced degradation based on Sn(II)-to-Sn(IV) oxidation, featuring the first step of oxygen adsorption on the surface and the sequential step of oxygen penetration via GB network; (**h**) Schematic illustration showing a generic method to stabilize Sn-based MHPs entailing stable adsorption of oxygen-resisting, multi-functional molecules; (**i**) Operational stabilities of perovskite-perovskite tandem

devices with and without CF3-PA passivation. Inset shows the multi-level interaction of CF3-PA via the particular Sn-defects in Sn-based MHPs in addition to various other generic surface defects in all MHPs. (**c, i**) is adapted from ref. [11,89] with the permission under the Springer-Nature. (**f**) is from ref. [87] with permission from the American Association for the Advancement of Science (AAAS).